



## NRC Publications Archive (NPArc) Archives des publications du CNRC (NPArc)

### **Signal attenuation and box-counting fractal analysis of optical coherence tomography images of arterial tissue**

Popescu, Dan P.; Fluerau, Costel; Mao, Youxin; Chang, Shoude; Sowa, Michael G.

#### **Publisher's version / la version de l'éditeur:**

*Biomedical Optics Express*, 1, 1, pp. 268-277, 2010-08-02

#### **Web page / page Web**

<http://dx.doi.org/10.1364/BOE.1.000268>

<http://nparc.cisti-icist.nrc-cnrc.gc.ca/npsi/ctrl?action=rtdoc&an=17673519&lang=en>

<http://nparc.cisti-icist.nrc-cnrc.gc.ca/npsi/ctrl?action=rtdoc&an=17673519&lang=fr>

Access and use of this website and the material on it are subject to the Terms and Conditions set forth at

[http://nparc.cisti-icist.nrc-cnrc.gc.ca/npsi/jsp/nparc\\_cp.jsp?lang=en](http://nparc.cisti-icist.nrc-cnrc.gc.ca/npsi/jsp/nparc_cp.jsp?lang=en)

READ THESE TERMS AND CONDITIONS CAREFULLY BEFORE USING THIS WEBSITE.

L'accès à ce site Web et l'utilisation de son contenu sont assujettis aux conditions présentées dans le site

[http://nparc.cisti-icist.nrc-cnrc.gc.ca/npsi/jsp/nparc\\_cp.jsp?lang=fr](http://nparc.cisti-icist.nrc-cnrc.gc.ca/npsi/jsp/nparc_cp.jsp?lang=fr)

LISEZ CES CONDITIONS ATTENTIVEMENT AVANT D'UTILISER CE SITE WEB.

Contact us / Contactez nous: [nparc.cisti@nrc-cnrc.gc.ca](mailto:nparc.cisti@nrc-cnrc.gc.ca).



# Signal attenuation and box-counting fractal analysis of optical coherence tomography images of arterial tissue

Dan P. Popescu,<sup>1,\*</sup> Costel Flueraru,<sup>2</sup> Youxin Mao,<sup>2</sup> Shoude Chang,<sup>2</sup>  
and Michael G. Sowa<sup>1</sup>

<sup>1</sup>National Research Council of Canada, Institute for Biodiagnostics, 435 Ellice Avenue, Winnipeg, MB, R3B 1Y6; Canada

<sup>2</sup>National Research Council of Canada, Institute for Microstructural Sciences, 1200 Montreal Road, Ottawa, ON, K1A 0R6; Canada

\*dan.popescu@nrc-cnrc.gc.ca

**Abstract:** The sensitivity of optical coherence tomography images to sample morphology is tested by two methods. The first method estimates the attenuation of the OCT signal from various regions of the probed tissue. The second method uses a box-counting algorithm to calculate the fractal dimensions in the regions of interest identified in the images. Although both the attenuation coefficient as well as the fractal dimension correlate very well with the anatomical features of the probed samples; the attenuation method provides a better sensitivity. Two types of samples are used in this study: segments of arteries collected from atherosclerosis-prone Watanabe rabbits (WHHL-MI) and healthy segments of porcine coronary arteries.

©2010 Optical Society of America

**OCIS codes:** (170.4500) Optical coherence tomography; (170.6935) Tissue characterization; (170.3880) Medical and Biological Imaging; (030.5770) Roughness.

---

## References and links

1. M. Shiomi, T. Ito, S. Yamada, S. Kawashima, and J. Fan, "Development of an animal model for spontaneous myocardial infarction (WHHLMI rabbit)," *Arterioscler. Thromb. Vasc. Biol.* **23**(7), 1239–1244 (2003).
2. C. Flueraru, H. Kumazaki, S. Sherif, S. Chang, and Y. Mao, "Quadrature Mach-Zehnder interferometer with application in optical coherence tomography," *J. Opt. A, Pure Appl. Opt.* **9**(4), L5–L8 (2007).
3. Y. Mao, S. Chang, S. Sherif, and C. Flueraru, "Graded-index fiber lens proposed for ultrasmall probes used in biomedical imaging," *Appl. Opt.* **46**(23), 5887–5894 (2007).
4. S. H. Yun, G. J. Tearney, J. F. de Boer, N. Iftimia, and B. E. Bouma, "High-speed optical frequency-domain imaging," *Opt. Express* **11**(22), 2953–2963 (2003).
5. D. Levitz, L. Thrane, M. Frosz, P. E. Andersen, C. B. Andersen, S. Andersson-Engels, J. Valanciunaite, J. Swartling, and P. Hansen, "Determination of optical scattering properties of highly-scattering media in optical coherence tomography images," *Opt. Express* **12**(2), 249–259 (2004).
6. J. M. Schmitt, S. H. Xiang, and K. M. Yung, "Speckle in optical coherence tomography," *J. Biomed. Opt.* **4**(1), 95–105 (1999).
7. B. Karamata, M. Laubscher, M. Leutenegger, S. Bourquin, T. Lasser, and P. Lambelet, "Multiple scattering in optical coherence tomography. I. Investigation and modeling," *J. Opt. Soc. Am. A* **22**(7), 1369–1379 (2005).
8. J. W. Goodman, *Laser Speckle and Related Phenomena* (Berlin Springer, 1984), Chap. 3 & 5.
9. J. W. Goodman, "Some fundamental properties of speckle," *J. Opt. Soc. Am.* **66**(11), 1145–1150 (1976).
10. D. J. Faber, F. J. van der Meer, M. C. Aalders, and T. G. van Leeuwen, "Quantitative measurement of attenuation coefficients of weakly scattering media using optical coherence tomography," *Opt. Express* **12**(19), 4353–4365 (2004).
11. C. Flueraru, D. P. Popescu, Y. Mao, S. Chang, and M. G. Sowa, "Added soft tissue contrast using signal attenuation and the fractal dimension for optical coherence tomography images of porcine arterial tissue," *Phys. Med. Biol.* **55**(8), 2317–2331 (2010).
12. W. C. Kuo, M. W. Hsiung, J. J. Shyu, N. K. Chou, and P. N. Yang, "Assessment of arterial characteristics in human atherosclerosis by extracting optical properties from polarization-sensitive optical coherence tomography," *Opt. Express* **16**(11), 8117–8125 (2008).
13. S. S. Chen, J. M. Keller, and R. M. Crownover, "On the Calculation of Fractal Features from Images," *IEEE Trans. Pattern Anal. Mach. Intell.* **15**(10), 1087–1090 (1993).

14. A. I. Penn, and M. H. Loew, "Estimating fractal dimension with fractal interpolation function models," *IEEE Trans. Med. Imaging* **16**(6), 930–937 (1997).
  15. P. Kotowski, "Fractal dimension of metallic fracture surface," *Int. J. Fract.* **141**(1-2), 269–286 (2006).
- 

## 1. Introduction

Atherosclerosis was once exclusively thought of as an occlusive disease where plaque accumulation on the arterial walls resulted in the narrowing of the arterial lumen. As our knowledge of atherosclerosis evolves, interest has shifted from the simple model of luminal narrowing towards complex biological processes occurring under the luminal surface. This interest induced the need for novel techniques able to image beneath the luminal surface of the artery. Optical coherence tomography (OCT) seems to be a natural candidate for imaging structures located under the luminal surface. OCT has an axial resolution that is determined by the coherence length of the light source, which usually is less than 10  $\mu\text{m}$ . Micrometer range resolution allows for the investigation of morphological details within the arterial wall not resolved by other techniques currently used for vascular imaging. Although a lot of information can be extracted from the visual inspection of an OCT image there is a need to analyze the data beyond the raw information provided by a simple image. Usually, visual inspection of an OCT image is a subjective procedure which is limited when there are small differences in the optical refraction indexes of various arterial components. For such cases, reliable quantitative parameters need to be identified in order to improve the sensitivity and the specificity in detecting and distinguishing vascular pathologies. There are two types of parameters that are the focus of this study. The first parameter considered is the attenuation of the OCT signal through various regions of interest (ROIs) within the probed samples. The other parameter class consists of the calculated fractal dimensions of recorded signal texture from ROIs within OCT images. The samples used for this study are segments of left descending coronary arteries harvested from healthy pigs and the descending aorta from atherosclerosis-prone Watanabe heritable hyper-lipidemic (WHHL-MI) rabbits [1].

## 2. Swept-source optical coherence tomography system and image acquisition

The OCT images for this study were acquired using a 3x3 Mach-Zehnder quadrature interferometer with a swept-source. The system has been described in detail elsewhere [2]. The swept source (HSL2000, Santac) has a central wavelength of 1320 nm and a full scan wavelength range of 110 nm. Its coherence length (in air) is 7  $\mu\text{m}$ . The light exiting the sample arm was focused onto the sample through ball-lens single mode fibers whose design and fabrication were described in a previous publication [3]. The whole probe head ensemble had the following specifications: working distance 1.1 mm, depth of field 0.9 mm and spot size 28.2  $\mu\text{m}$ . The total optical power illuminating the sample was approximately 5 mW. The balanced detection output is recorded with a digitizer (Alazartech) at a 100 MHz sampling rate. After the records were re-sampled to equal frequency intervals, an inverse Fourier transform was performed. The end result was a depth profile (A-scan), which is the dependence on depth of the sample reflectance. The standard OCT image (B-scan) used for this study contains 900 A-scans, which amounts to a scanning width of 3 mm. Overall, the Mach-Zehnder OCT system had a measured sensitivity of 107 dB. There is an exponential falloff of sensitivity with depth for the swept source which is related to the limited instantaneous lineshape of its laser [4]. This effect can be explained as a decreasing visibility of the higher frequency fringes which are back-reflected from deeper locations within the sample. The sensitivity falloff parameter is defined as the position where the sensitivity decreases by 6 dB and the measured sensitivity falloff of the home-built OCT system used in this report was 2.8 mm. Since the measured sensitivity falloff of our system was larger than the investigated ROI depths, there was not necessary to take into consideration this effect when analysis of OCT data acquired during this investigation was performed.

### 3. Sample preparation and image acquisition

Segments of artery were snap-frozen immediately after they were harvested and stored at  $-80^{\circ}\text{C}$  until the time of imaging. The acquisition of OCT images was conducted at room temperature after samples were allowed a short period of thawing also at room temperature. We have investigated two types of arterial tissues: one type harvested from healthy pigs and the other from atherosclerosis-prone Watanabe (WHHL-MI) rabbits. This type of rabbit spontaneously develops atherosclerotic plaques resembling key aspects of the human clinical condition [1]. Testing was carried out in two geometries: one with the lumen side and the other with the external adventitia exposed to the probing beam, respectively. For the first testing geometry, the arterial samples were cut open along the direction of blood flow. For the second testing geometry the arterial samples were not cut open. In this case samples had their serosa and adventitia layers exposed directly to the probing beam and the collapsed lumen could be identified in the OCT images.

An example of an OCT image collected from a portion of porcine coronary left descending artery shown in Fig. 1. This sample has the lumen surface exposed to the OCT probing beam. Detailed anatomical features of the artery are clearly displayed; starting from the top of the image, the intima, media and adventitia are resolved. This OCT image (i.e. B-scan) is composed from a number of 900 A-scans, which amount to a 3-mm physical width on the scanned sample. Correspondingly, the depth of the image (i.e. the vertical size) is about 1.5 mm.

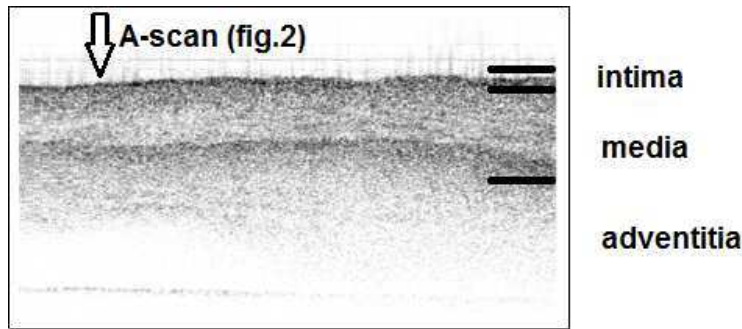


Fig. 1. An OCT image of a segment of an asymptomatic porcine artery. Starting from the top, the intima, media and adventitia layers can be distinguished in this image. There are a total of 900 A-scans composing the image. The image size is 1.5 (depth) x 3 mm<sup>2</sup>. The arrow indicates the position of the 150-th A-scan, which is used as an example in Fig. 2. The straight line observed above the sample surface in the OCT image marks the air/isotonic saline interface.

### 4. Attenuation of the OCT signal

As light penetrates into the artery, the OCT signal is increasingly attenuated due to the overall effect of scattering, absorption, modification of the polarization state of the probing light and coherence loss. The rate of attenuation of the OCT signal while it propagates within the sample is potentially a parameter of interest because tissues with different optical properties attenuate the OCT signal differently [5]. In an individual A-scan the recorded signal is very noisy, as it can be seen in Fig. 2, which displays the 150-th A-scan from OCT image shown in Fig. 1. Therefore, the determination of changes in the attenuation rate along the depth profile, which mark signal propagation from one type of tissue to another, would be very problematic. A noisy A-scan profile is a common feature for OCT measurements probing highly scattering environments. It is attributable to the random distribution of discrete scattering centers along the depth probed by the light, to the speckle noise generated by multiple scattering of light, and to the electronic noise plaguing the detection system [6,7].

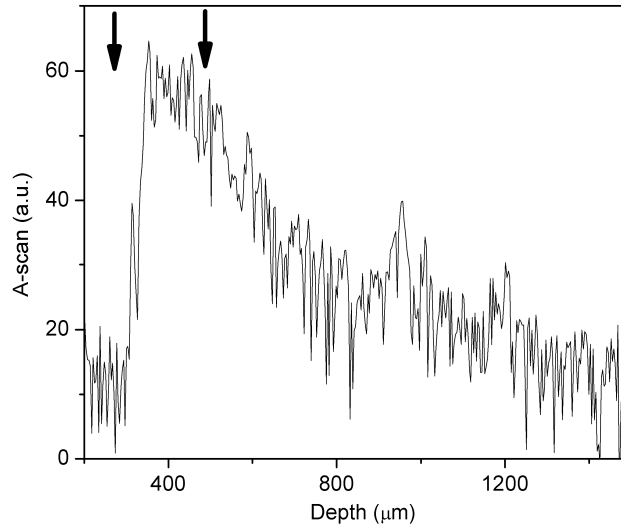


Fig. 2. An example of an A-scan, i.e. the reflectivity profile versus depth. The A-scan profile is noisy and does not allow for a reliable estimation of its attenuation with depth. The arrows mark the portion of the A-scan section selected in Fig. 4.

In order to overcome this problem and to obtain a smooth profile that ensures a reliable estimation of an attenuation coefficient, a summation of adjacent A-scans had to be performed thus obtaining a compounded profile. In an OCT system the detection is based on light interference therefore the signal is coherent. By adding a number  $N$  of un-correlated adjacent A-scans the signal part carrying genuine information from the sample (i.e. signal generated through a single light back-scattering event) is increased  $N$  times, while the part of the signal generated from coherent speckle noise increases only by  $N^{1/2}$  [8,9]. Therefore, in a compounded profile the amount of coherent noise decreases with respect to the amount of information-carrying signal.

The compounded profile derived from this summation procedure as applied to the A-scans that compose the OCT image from Fig. 1 is demonstrated in Fig. 3. Now, the interfaces which separate various layers in the OCT image are easily observed in the compounded profile and are marked by reflectivity peaks followed by changes in the slope of the profile. The parameters of interest are the attenuation coefficients along various sections of the compounded profile. Based on the single scattering model their values can be calculated by numerically fitting the distinct sections of the compounded profile with exponential-like functions. The procedure used was similar with one of the numerical models described in reference [10]. Each selected portion of compounded profile was independently fit with a simple exponential function. There were two free parameters used for fitting: a free multiplier and the attenuation rate of the signal along the selected portion of the compounded profile. Only fits with correlation factors  $R^2$  higher than 0.85 were considered reliable and used in this report. Graphic exemplification of this procedure is displayed in Fig. 3 where straight lines indicate various portions of the profile which were independently fit with exponential functions.

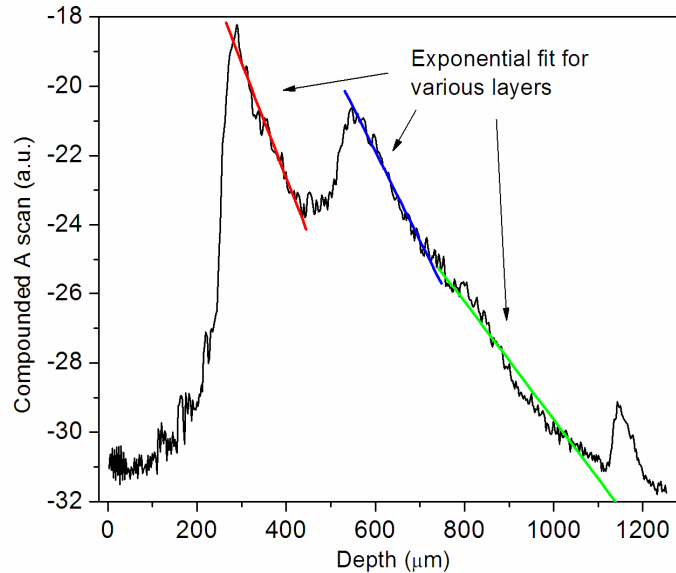


Fig. 3. Compounded profile corresponding to the OCT image from Fig. 1. Numerical fits corresponding to different layers are also shown.

By applying the signal attenuation method, features which were not clearly evident in the initial OCT images were identified. For example, in the medial layer of the porcine artery we identified two sub-layers each bearing its own class of attenuation coefficients. The change in the attenuation of the OCT signal was attributed to a change in the orientation of the elastin fiber bundles in the medial layer [11]. It is known that the wall of a healthy artery has a well ordered elastin fiber network that imparts elasticity to the vessel allowing it to contract and expand during the cardiac cycle. This leads to a directional anisotropy of the optical properties of the medial layer of the porcine coronaries, which is reflected in the attenuation of the OCT signal. These types of morphological-induced optical anisotropies in arterial tissues could be also emphasized through polarization-sensitive OCT [12].

The media layer sections that showed different elastin fiber orientation could not be easily differentiated by a visual examination of the OCT image. However, the two sub-sections of the media layer in the porcine left descending coronary arteries were made evident and quantifiable by measuring the attenuation coefficient of the compounded signal. The average values obtained for the attenuation coefficients of the OCT signal propagated through the media were as follows (starting from the sub-layer that borders the tunica intima):  $4.60 \pm 0.29 \text{ mm}^{-1}$  and  $5.63 \pm 0.05 \text{ mm}^{-1}$  (when the scanning occurs along the direction of blood flow), and  $1.59 \pm 0.19 \text{ mm}^{-1}$  and  $8.31 \pm 0.09 \text{ mm}^{-1}$  (scanning perpendicular to the flow). Meanwhile, the media sub-layers were not visible in the OCT images acquired from the WHHL-MI rabbit arteries but they were signaled by the attenuation coefficients of the corresponding compounded profiles. For this class of samples, when the scanning occurs perpendicular to the direction of blood flow the following values are obtained for the attenuation of signal propagating through the media sub-layers:  $1.77 \pm 0.02 \text{ mm}^{-1}$  (sub-layer adjacent to the tunica intima) and  $2.38 \pm 0.04 \text{ mm}^{-1}$  (sub-layer adjacent to adventitia). Unlike the media, the adventitia layer has a homogeneous structure characterized by single OCT signal attenuation:  $1.19 \pm 0.02 \text{ mm}^{-1}$  (porcine, scanned along the blood flow),  $1.36 \pm 0.03 \text{ mm}^{-1}$  (porcine, scanned across the blood flow) and  $0.81 \pm 0.07 \text{ mm}^{-1}$  (rabbit, scanned across the blood flow). The intima layers were too thin to obtain numerical fits with small errors.

## 5. Fractal analysis: the box-counting method

Another important feature that could be used to differentiate among various ROI's that appear in an OCT image is the texture of the signal as it was recorded within the image. Texture refers to the physical appearance of a region and the signal texture in an OCT image should contain information about sample morphology embedded within its speckle. Fractal analysis is the method of choice for characterizing textures and one of its variants, the box-counting technique, was used in this study to calculate fractal values corresponding to each A-scan portion that is part of an ROI. Detailed description of the theoretical background and the mathematical algorithms for box-counting fractal analysis are provided elsewhere [13,14].

The fractal analysis started by identifying an ROI within an OCT image. Subsequently, the box-counting algorithm was used for calculating a fractal dimension corresponding to each A-scan portion contained within that ROI. As an example, we consider a portion of the A-scan shown in Fig. 2. This A-scan portion is detailed in Fig. 4 where it horizontally spans over 64 pixels corresponding to an optical depth of 275  $\mu\text{m}$ . The location of this portion within the initial A-scan is marked with arrows in Fig. 2. The first step in calculating the fractal dimension of this A-scan portion was to "cover" it with a uniform set of square boxes, each of side length  $l_i$ . Figure 4 shows the case when the A-scan portion of interest was covered with 20 square boxes, each square being 16 pixels wide ( $\sim 69 \mu\text{m}$ 's along the x-axis). The second step of the algorithm counts the number of non-empty boxes  $N_i$ , i.e. the boxes containing signal from the selected A-scan profile. The number of non-empty boxes is ten in the example provided in Fig. 4.

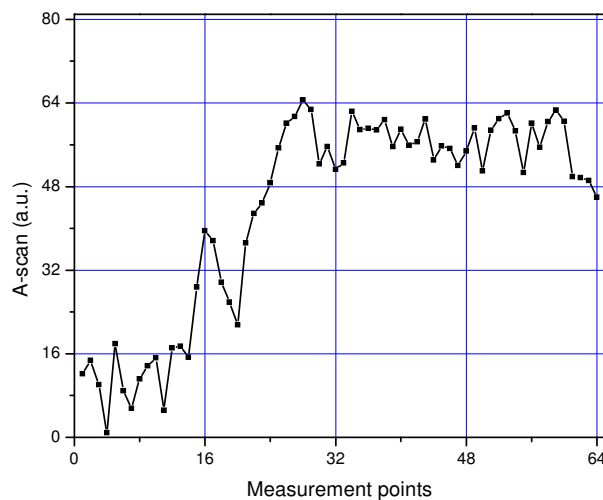


Fig. 4. The portion from the A-scan shown in Fig. 2 which is contained within the arrows. The number of measurement points (pixels) is limited to 64 corresponding to a depth of about 275  $\mu\text{m}$ . The box size shown in this example is 20 and a number of ten boxes containing signal (non-empty) can be counted. This partition corresponds to one point in Fig. 5 describing the fractal dimension calculation.

These two steps were repeated for different box sizes while the box sides were decreased each time by a factor of two. The algorithm started with the first box covering the entire portion of the A-scan (64 pixels in this example) and continued until the profile was covered with two-pixel wide boxes. Two pixels corresponded to a length of  $\sim 8.6 \mu\text{m}$ , which is very close to the coherence length of the OCT system. Finally, the box-counting dimension was calculated as the slope of the line obtained by fitting the number of non-empty boxes  $N_i$

against box side length  $l_i$  on a log–log scale as shown in Fig. 5. The fractal dimension of any A-scan profile can be any fractional number between 1, which is the fractal dimension of a straight line, and 2, value which constitutes the fractal dimension of a flat plane.

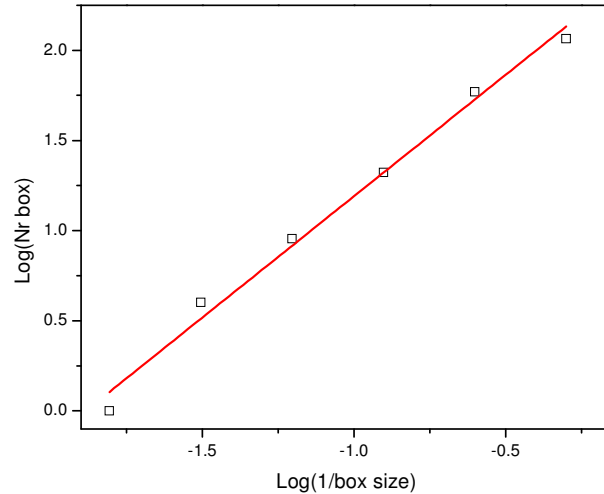


Fig. 5. The slope of the linear fit in log-log scale of number of boxes versus box size is the fractal dimension. The slope was calculated over six points corresponding to six box sizes from 2 to 64 pixels. The minimum box sizes was  $8.6 \mu\text{m}$ , which corresponded to the axial (spatial) resolution of the OCT image while the maximum box size was defined by the optical width of the chosen ROI,  $275 \mu\text{m}$ .

Two examples of full ROIs are indicated in Fig. 6 by the rectangular contours. Both ROIs were selected to cover a depth of 64 pixels ( $275 \mu\text{m}$  in the axial direction) and were extended to include the whole image width, 900 A-scans in this case.

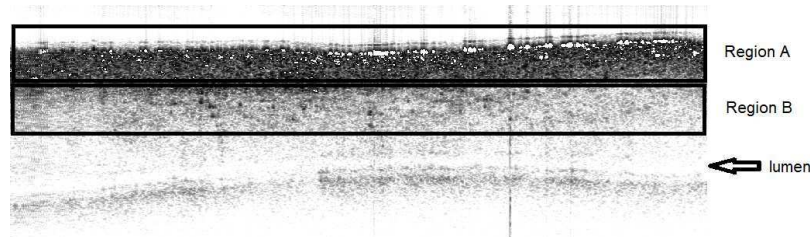


Fig. 6. An OCT image of a portion of WHHM-LI rabbit artery. The image size is 2 (depth) mm x 3 mm (width) or 300 x 900 pixels. The rectangular contours indicate examples of two ROIs extending across the whole width of the image, 900 pixels. Each ROI has a depth of 64 pixels ( $275 \mu\text{m}$ ).

The box-counting algorithm described above provides a corresponding fractal value for each A-scan portion contained within a selected ROI. By using ROIs similar to the ones selected in Fig. 6, 900 fractal dimensions were obtained for each ROI. In Fig. 7a there is a histogram plot of all the fractal values from region A with a corresponding Gaussian numerical fit. The bin size used to calculate the distribution of fractal dimension for an entire ROI was defined by the maximum standard deviation obtained from all the linear fittings of log-log graphs corresponding to all A-scan portions contained within that ROI. The peak of the Gaussian fit indicated an average fractal value for that particular ROI while the width of

the Gaussian fit could be used as a measure for the homogeneity of the tissue portion covered by the ROI (region A in this case).

Figure 7b was obtained in a similar way for region B, also shown in Fig. 6. Region B has the same size as region A but is displaced 64 pixels deeper into the sample. Can be noted that the average fractal value (the Gaussian peak) changed from one ROI to the other and, more importantly, the Gaussian width decreased in Fig. 7b. This was the result of having different OCT signal textures within the two selected ROI's. The first ROI contains a significant portion of empty space, i.e. portion above the sample surface, while the second ROI contains mostly signal generated from inside the sample. This example clarifies the potential of using the width of the Gaussian fit as a classification tool for the tissue portions covered by various ROI's..

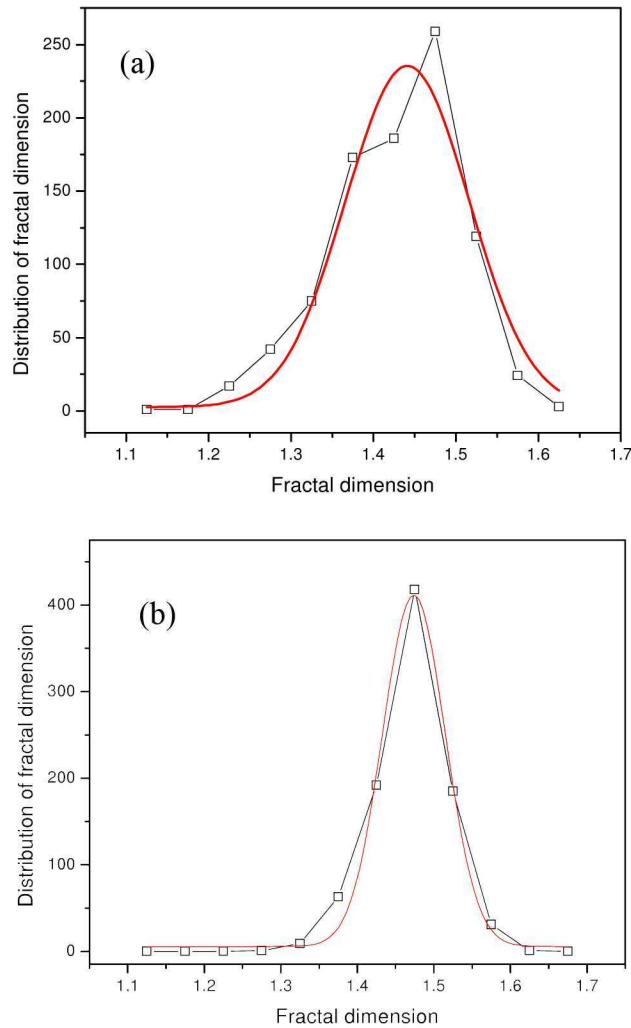


Fig. 7. (a) The histogram of the fractal dimensions calculated for the region contained within the rectangle from Fig. 6 (region A). The histogram is fitted with a Gaussian profile. (b) Histogram of the fractal dimension calculated for the ROI obtained after a 64-pixel displacement as indicated in Fig. 6 (region B). This histogram is fitted with a Gaussian profile narrower than the one from Fig. 7a indicating that within this ROI are less OCT signal texture types.

For all investigated samples, Gaussian numerical fits were applied to the corresponding histograms with correlation factors  $R^2$  0.93 or higher. For the rabbit arteries, the average Gaussian profile peaks occurred at 1.441 (adventitia) and at 1.472 (media). Meanwhile the corresponding widths of the Gaussian curves were 0.149 (adventitia) and 0.081 (media), values that demonstrated narrow distributions around the central peaks (average fractal values) for samples belonging to the same type of tissue, i.e. to either adventitia or media layer. Sometimes secondary peaks, three to six times smaller than the amplitude of the main peak, appeared in the histograms when a selected ROI was partially covering a location with a different signal texture. The same procedure was used to calculate the fractal dimensions in the OCT images from the porcine left descending coronaries. The values obtained for the average fractal dimensions were 1.194 (the first sub-layer of the media), 1.267 (the second sub-layer) and 1.277 (adventitia). The corresponding widths of the Gaussian distributions were as follows: 0.085 (the first sub-layer), 0.067 (the second sub-layer) and 0.054 (adventitia).

Kotowski investigated the fractal dimension of metallic fractured surfaces and demonstrated that the fractal roughness (or dimension) shifts as the length of the surface profile increase [15]. By plotting the fractal dimension versus length of the surface profile, he found a plateau called the characteristic fractal value. In the case of OCT images, the length corresponding to the surface profile is the depth of the A-scan quantity. Since the penetration depths of OCT scans are limited, a similar analysis with the one proposed by Kotowski is not applicable. This indicates that the characteristic fractal dimension regime may not be reached when applying the box-counting method on OCT images. However, in the OCT case, by applying the algorithm to A-scans which have the same depths makes the comparison of the fractal dimensions obtained for different regions relevant even when the characteristic fractal values are not reached.

## 6. Conclusion

Biological and morphological variations in arterial tissues generate changes in the optical properties of tissue, such as in light scattering, absorption and refractive index, which in turn affect the OCT signal. Detection of this altered signal in state-of-the-art OCT systems leads to high-quality OCT images, which capture many of the structural characteristics of the sample. Despite the fidelity of images, OCT analysis has to progress beyond the subjective visual inspection of high-quality images toward more quantitative methods. Two methods were proposed in this report: one based on determining the attenuation coefficient of the OCT signal as it propagated within the probed sample and the other based on calculation of average fractal dimensions using a box-counting algorithm applied to specific ROIs in OCT images. Two types of arterial tissue samples were used in this investigation: healthy porcine left descending coronary arteries and pieces of descending aortas harvested from atherosclerosis-prone Watanabe heritable hyper-lipidemic (WHHL-MI) rabbits. The method based on using the attenuation coefficient was not only able to distinguish the gross anatomical features of the arterial wall but was also able to point toward more subtle anatomical features not apparent on the original OCT images. For example, the two sub-layers of the tunica media where the smooth elastin fibers have different orientations could be distinguished based on different OCT signal attenuations. In addition, we have shown that the second method, box-counting, could provide two parameters suitable to be used for sample characterization: the average fractal value and the width of the Gaussian fit. These parameters could be used for further improvement in soft-tissue differentiation. Different fractal dimensions were obtained for different layers and sub-layers of the investigated samples. Although more studies are needed, there is a strong indication that fractal analysis could be used to further refine the classification of various regions within OCT images acquired from anatomically complex biological samples. In addition, a procedure which makes use of both methods could be envisioned. The box counting method could be used in a preliminary step to identify areas

with similar signal textures within OCT images. In a follow-up step, the attenuation coefficient for the OCT signal within such a fractal-identified region of interest could be extracted.